physica status solidi rrl
www.pss-rapid.com

Interface Structure and Doping of Chemical Vapor Deposition-Grown MoS_2 on 4H–SiC by Microscopic Analyses and Ab Initio Calculations

Salvatore Ethan Panasci, Ioannis Deretzis, Emanuela Schilirò, Antonino La Magna, Fabrizio Roccaforte, Antal Koos, Béla Pécz, Simonpietro Agnello, Marco Cannas, and Filippo Giannazzo**

The interface structure and electronic properties of monolayer (1L) MoS_2 domains grown by chemical vapor deposition on 4H–SiC(0001) are investigated by microscopic/spectroscopic analyses combined with ab initio calculations. The triangular domains are epitaxially oriented on the (0001) basal plane, with the presence of a van der Waals (vdW) gap between 1L–MoS_2 and the SiC terraces. The high crystalline quality of the domains is confirmed by photoluminescence emission. Furthermore, a very low tensile strain ($\varepsilon \approx 0.03\%$) of 1L–$MoS_2$, consistent with the small in-plane lattice mismatch, and a p-type doping of $(0.45 \pm 0.11) \times 10^{13}$ cm^{-2}, is evaluated by Raman mapping. Density functional theory (DFT) calculations of the MoS_2/4H–SiC(0001) system are also performed, considering different levels of refinement of the model: 1) the simple case of the junction between Si-terminated SiC and MoS_2, showing a covalent bond between the Si–S atoms and n-type doping of MoS_2; 2) the complete passivation of Si dangling bonds with a monolayer (1 ML) of oxygen atoms, resulting in a vdW bond with $d_{Si-S} \approx 3.84$ Å bond length and p-type doping of MoS_2; and 3) partial (¼ ML and ½ ML) oxygen coverages of the 4H–SiC surface, resulting in intermediate values of d_{Si-S} and doping behavior.

1. Introduction

Transition metal dichalcogenides (TMDs) are a class of 2D materials described by the general formula MX_2, where M are transition metal atoms (Mo,W,.) and X is a chalcogen (S, Se, and Te). TMDs are featured by strong in-plane bonds between the constituent atoms (X–M–X) and weak van der Waals (vdW) interactions between the stacked layers.[1] Molybdenum disulfide (MoS_2) is the most investigated among TMDs, due to its abundance in nature and the chemical stability at room temperature. In particular, the 2H–MoS_2 semiconductor phase exhibits a tunable bandgap as a function of the thickness, with a transition from an indirect bandgap of 1.2 eV for few-layer MoS_2 to a direct bandgap of 1.8–1.9 eV for monolayer (1L) MoS_2.[2,3] The combination of chemical stability, semiconductor behavior, and bandgap tunability in the near-infrared–visible range makes MoS_2 very appealing for potential applications in electronics, optoelectronics, sensing and photocatalysis.[4–7] Furthermore, its dangling bonds free surface provides the opportunity to fabricate vdW heterostructures both in combination with other 2D materials (2D/2D heterostructures) and with bulk semiconductors (2D/3D semiconductor heterostructures).[8,9] In this context, significant research efforts have been recently directed on the integration of the MoS_2 with wide-bandgap (WBG) semiconductors, such as silicon carbide (4H- and 6H–SiC), gallium nitride (GaN), and related group-III nitrides (AlN and AlGaN alloys), with the aim of

S. E. Panasci, I. Deretzis, E. Schilirò, A. La Magna, F. Roccaforte, F. Giannazzo
Consiglio Nazionale delle Ricerche - Istituto per la Microelettronica e Microsistemi (CNR-IMM)
95121 Catania, Italy
E-mail: ioannis.deretzis@imm.cnr.it; filippo.giannazzo@imm.cnr.it

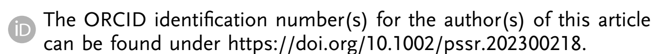
The ORCID identification number(s) for the author(s) of this article can be found under https://doi.org/10.1002/pssr.202300218.

© 2023 The Authors. physica status solidi (RRL) Rapid Research Letters published by Wiley-VCH GmbH. This is an open access article under the terms of the Creative Commons Attribution License, which permits use, distribution and reproduction in any medium, provided the original work is properly cited.

DOI: 10.1002/pssr.202300218

A. Koos, B. Pécz
Centre for Energy Research
Institute of Technical Physics and Materials Science
1121 Budapest, Hungary

S. Agnello, M. Cannas
Department of Physics and Chemistry Emilio Segrè
University of Palermo
90123 Palermo, Italy

S. Agnello
ATEN Center
University of Palermo
90128 Palermo, Italy

demonstrating advanced photodetectors operating both in the visible and in the ultraviolet (UV) spectral range[10–13] and innovative heterojunction diodes for fast switching and low-power consumption electronics.[14–18] The hexagonal structure of 4H–SiC and GaN and the very low lattice mismatch with MoS_2 on the basal plane (≈2.9% in the case of 4H–SiC and < 1% in the case of GaN) favor the direct epitaxial growth of MoS_2 layers on these substrates. The nucleation and growth of highly oriented and nearly unstrained triangular MoS_2 domains are obtained on the GaN(0001) basal plane by chemical vapor deposition (CVD) at temperatures of 700–800 °C.[8] On the other hand, a large variety of MoS_2 configurations has been reported by CVD on the surface of 6H- or 4H–SiC(0001) depending on the growth conditions and the SiC miscut angle (i.e., on-axis or off-axis surface). These include uniform planar films (suitable for electronic applications)[12] and vertically standing triangular flakes exposing MoS_2 edges (more suitable for catalytic applications).[19] In the case of planar MoS_2 on these SiC surfaces, studies of the early growth stages, providing information on the rotational alignment of MoS_2 domains with respect to the (0001) basal plane, are still missing and would be highly desirable. Furthermore, a deeper understanding of the interface bond, strain, and doping for CVD-grown MoS_2 on 4H–SiC(0001) is required, both by microscopic characterizations and ab initio calculations, to exploit the potentialities of this system for electronic applications. Recently, ab initio computational studies of the equilibrium configurations for 1L–MoS_2 heterostructures with the Si-terminated SiC(0001) surface have been reported, showing that the most energetically stable configuration is the one where S atoms are located on top of Si atoms with an equilibrium distance $d_{Si–S} = 2.21$ Å.[20] Such a small $d_{Si–S}$ value indicates a strong (covalent-like) bond between MoS_2 and 4H–SiC(0001) in this idealized model of the heterostructure. In this context, further computational studies considering additional effects, such as the natural propensity of the Si-terminated 4H–SiC surface to be passivated by oxygen atoms, are required to provide a more realistic description of the 1L–MoS_2/4H–SiC system.

In this article, we investigated the interface structure and electronic properties of CVD-grown 1L–MoS_2 on 4H–SiC(0001), by combining microscopic and spectroscopic analyses with density functional theory (DFT) calculations. High-crystalline-quality triangular domains, mostly composed of 1L–MoS_2, were obtained on the surface of 4H–SiC(0001) 4° off-cut samples by CVD with S and MoO_3 vapors at 700 °C. Top-view scanning electron microscopy (SEM) analyses showed preferential orientation of these domains along specific directions, indicating an epitaxial relation with the (0001) basal plane, while cross-sectional scanning transmission electron microscopy (STEM) measurements demonstrated a conformal coverage of 1L–MoS_2 on the SiC terraces, with a vdW gap in between. A very low tensile strain ($\varepsilon \approx 0.03\%$) of 1L–$MoS_2$, consistent with the very low in-plane lattice mismatch, and p-type doping of $(0.45 \pm 0.11) \times 10^{13}$ cm^{-2} was evaluated by Raman analyses. To get an interpretation of these experimental results, DFT calculations of the equilibrium structure and electronic bands for the MoS_2/4H–SiC(0001) system were also performed, considering different levels of refinement of the model: 1) the simple case of the junction between Si-terminated SiC and MoS_2 showing covalent bonds with $d_{Si–S} = 2.24$ Å between the Si–S atoms and n-type doping of MoS_2; 2) the complete passivation of Si dangling bonds with a monolayer (1 ML) of oxygen atoms, resulting in a van der Waals bond with $d_{Si–S} \approx 3.84$ Å and p-type doping of MoS_2; and 3) partial (¼ ML and ½ ML) oxygen coverage of the 4H–SiC surface, resulting in intermediate values of $d_{Si–S}$ and doping behavior. Interestingly, the complete O-passivation of the Si-terminated 4H–SiC surface caused a rehybridization of the underlying carbon atoms from sp^3 to sp^2, which was found to be the origin of the p-type doping of 1L–MoS_2.

2. Results

A representative in-plane SEM image of the as-grown MoS_2 on 4H–SiC (0001) by CVD is reported in **Figure 1**a, showing the formation of triangular flakes with a 100–300 nm lateral size. Most of these flakes exhibit two preferential orientations, as illustrated by the red triangles at 0° and 180° with respect to the reference dashed line in the figure, suggesting the epitaxial growth of MoS_2 on hexagonal SiC with a high degree of rotational alignment. This aspect has been confirmed by an accurate statistical analysis of domains orientation, carried out on all MoS_2 triangles in the SEM image. The result of this analysis, reported in the histogram of Figure 1b, shows that the grown MoS_2 domains are almost equally distributed in two groups with orientations of 0°± 30° and 180°± 30°. The rotational alignment of MoS_2 domains on

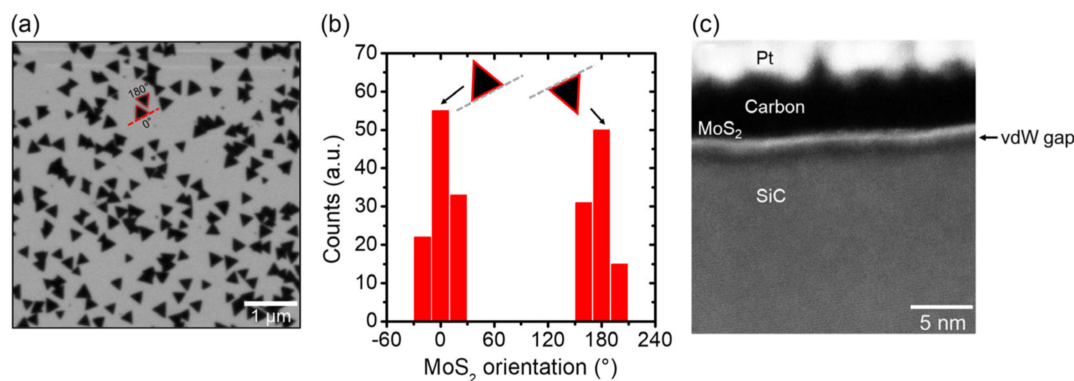

Figure 1. a) SEM image of the triangular MoS_2 flakes on the 4H–iC 4H–SiC(0001) surface and b) histogram of the MoS_2 triangles orientation. c) Cross-sectional HAADF–STEM image of the MoS_2/SiC heterostructure.

© 2023 The Authors. physica status solidi (RRL) Rapid Research Letters published by Wiley-VCH GmbH

18626270, 2023, 10, Downloaded from https://onlinelibrary.wiley.com/doi/10.1002/pssr.202300218 by CochraneItalia, Wiley Online Library on [01/11/2023]. See the Terms and Conditions (https://onlinelibrary.wiley.com/terms-and-conditions) on Wiley Online Library for rules of use; OA articles are governed by the applicable Creative Commons License

4H–SiC(0001) surface is beneficial for the reduction of grain boundaries in the continuous MoS_2 film formed by merging of the domains during longer CVD processes, as reported in previous works.[21,22] Figure 1c shows a cross-sectional STEM image collected in the high-angle-annular dark-field (HAADF) mode on one of these triangular domains. The intensity contrast in this imaging mode, related to the atomic number (Z), allows to clearly identify materials with different density, that is, the SiC substrate, the deposited MoS_2 layer, and a carbon thin film capped with Pt (used to protect MoS_2 during the lamella preparation by focused ion beam). In particular, the presence of 1L–MoS_2 conformal to the stepped surface of 4 -offcut 4H–SiC, with a vdW gap in between, is clearly resolved from this microscopic analysis, as indicated in Figure 1c.

Besides the HAADF–STEM analysis, chemical mapping by EDS was performed on the same cross-sectioned sample, as reported in the Figure S1, Supporting Information. This analysis shows an evident accumulation (above the background signal) of oxygen on the SiC surface, below the MoS_2 layer. This observation supports the DFT model of oxygen passivation of SiC surface, discussed in the final part of this article.

The high crystalline quality and the monolayer thickness of the as-grown MoS_2 domains on 4H–SiC were also confirmed by the observation of photoluminescence (PL) spectra, collected using a micro-PL setup and a laser excitation wavelength of 532 nm. **Figure 2** shows a representative PL spectrum, which exhibits a main emission peak at 1.87 eV, consistently with the typical observation of a direct-bandgap transition in single-layer MoS_2.[2,3,23] Furthermore, the deconvolution analysis revealed the presence of three contributions to the emission spectrum, that is, the exciton peaks A^0 (at 1.87 eV) and B (at 1.98 eV) and a trionic contribution A^- (at 1.79 eV), typically reported for high-crystalline-quality 1L–MoS_2.[23] It is worth mentioning that high defects density in single-layer MoS_2 results in a significant quenching of the PL intensity, associated with nonradiative recombination processes, and in the introduction of a specific defect-related peak (X_D) in the PL spectrum.[24,25] Thus, an intense PL emission and the absence of X_D contribution after the deconvolution analysis provide strong evidences of the high crystal quality of the CVD MoS_2 domains on 4H–SiC.

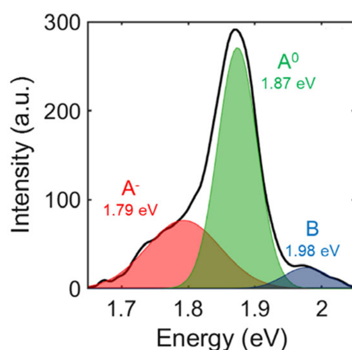

Figure 2. Micro-PL spectrum of as-grown MoS_2 on 4H–SiC. The deconvolution analysis allows to identify three spectral contributions, that is, the exciton peaks A^0 (at 1.87 eV) and B (at 1.98 eV) and the trionic contribution A^- (at 1.79 eV).

The thickness uniformity, strain, and doping of the CVD-grown MoS_2 on 4H–SiC were further investigated by Raman mapping. **Figure 3**a shows a representative Raman spectrum of as-grown MoS_2, where the characteristic peaks associated with the in-plane (E_{2g}) and out-of-plane (A_{1g}) MoS_2 vibrational modes are clearly identified. The two Raman peaks have been optimally fit by Lorentzian functions with a very small full width at half maximum i.e., ≈3.7 and 4.8 cm^{-1}, which confirms the high crystal quality of the MoS_2 domains. Furthermore, the deconvolution procedure revealed the presence of a very small defect-related LO(M) component at ≈379.9 cm^{-1},[26] probably associated with the edges of the triangular domains.

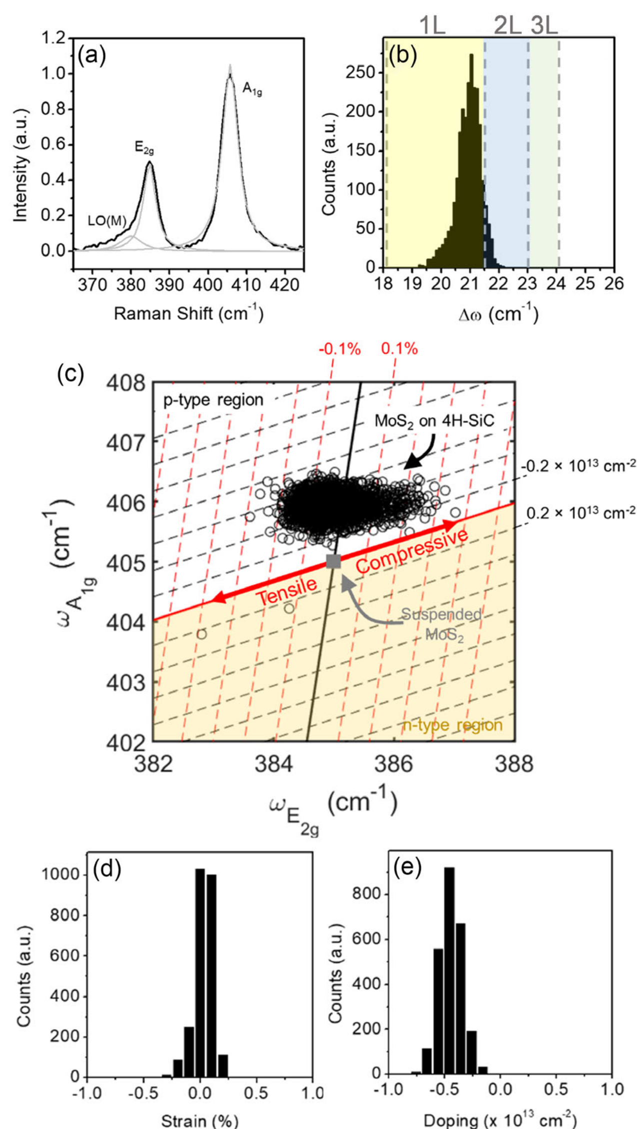

Figure 3. a) Raman spectrum of MoS_2 on 4H–SiC (black line), and deconvolution analysis (grey lines), showing the presence of the LO(M), E_{2g}, and A_{1g} peaks. b) Histogram of the frequency difference ($\Delta\omega = \omega_{A1g} - \omega_{E2g}$) between the two Raman peaks. c) Correlative E_{2g} versus A_{1g} plot showing the experimental positions obtained for the CVD-grown 1L–MoS_2 on 4H–SiC. Histogram of the deduced strain d) and doping e) values for the 1L–MoS_2 on 4H–SiC.

© 2023 The Authors. physica status solidi (RRL) Rapid Research Letters published by Wiley-VCH GmbH

18626270, 2023, 10, Downloaded from https://onlinelibrary.wiley.com/doi/10.1002/pssr.202300218 by CochraneItalia, Wiley Online Library on [01/11/2023]. See the Terms and Conditions (https://onlinelibrary.wiley.com/terms-and-conditions) on Wiley Online Library for rules of use; OA articles are governed by the applicable Creative Commons License

These results are comparable to the state-of-art MoS_2 obtained by CVD. The thickness uniformity of the MoS_2 domains was evaluated by Raman mapping from the frequency difference $\Delta\omega = \omega_{A1g}–\omega_{E2g}$ of the two Raman modes, which is commonly correlated to MoS_2 layer number.[27] The histogram in Figure 3b shows the statistical distribution of the $\Delta\omega$ values extracted from an array of 2500 Raman spectra. The number of MoS_2 layers corresponding to the different $\Delta\omega$ ranges is also reported on the top horizontal scale, indicating that the film is mostly composed of 1L–MoS_2 ($\Delta\omega$ between 18 and 21.5 cm^{-1}), with a small percentage of 2L–MoS_2 ($\Delta\omega$ between 21.5 and 23 cm^{-1}).

The distribution of $\Delta\omega$ values for 1L–MoS_2 can be correlated to variations of MoS_2 strain and doping induced by the growth conditions or by interaction with the substrate.[28–30] In particular, the strain (ε) and doping (n) parameters are related to the frequencies of the E_{2g} and A_{1g} peaks by the following equation

$$\omega_m = \omega_m^0 - 2\gamma_m \omega_m^0 \varepsilon + k_m n \quad (1)$$

where ω_m ($m = E_{2g}$ or A_{1g}) represents the measured frequencies of the vibrational modes, ω_m^0 the values for the ideal unstrained and undoped monolayer MoS_2, the parameters γ_m (Grüneisen parameters) rule peaks' shift as a function of the strain,[31,32] while k_m rules the shift as a function of doping.[33] In particular, $\omega_{E2g}^0 = 385\ cm^{-1}$ and $\omega_{A1g}^0 = 405\ cm^{-1}$ literature values for a suspended MoS_2 membrane[34] have been taken as good approximations for the unstrained/undoped MoS_2 case.

Equation (1) can be graphically solved by the correlative plot in Figure 3c, where the red and black continuous lines represent the theoretical strain and doping lines, respectively, and their intersection (grey square) is the (ω_{E2g}^0, ω_{A1g}^0) value for suspended 1L–MoS_2. The two red arrows along the strain line indicate the direction for the tensile and compressive strain, while the yellow and white areas in the ω_{A1g} versus ω_{E2g} diagram indicate the n-type and p-type doping regions respectively. Furthermore, the black and red dashed lines serve as guides for the eye to estimate the ε and n values, with the separation between dashed red and black lines corresponding to step of $\pm 0.1\%$ and $\pm 0.2 \times 10^{13}\ cm^{-2}$ for the strain and doping, respectively. The black points in Figure 3c represent the experimental peak frequencies deduced from the 2500 Raman spectra measured on the 1L–MoS_2/4H–SiC. The cloud of points falls in the white area of the plot, corresponding to the p-type doping region. Furthermore, they are nearly equally distributed around the doping line, corresponding to quasiunstrained MoS_2. Figure 3d,e shows the histograms of the biaxial strain and doping values evaluated from the correlative plot. The strain distribution (Figure 3d) exhibits a peak at $\varepsilon = 0.03\%$ and a standard deviation of 0.09%. These very low strain values are consistent with the low in-plane lattice mismatch between MoS_2 and 4H–SiC. Furthermore, from doping distribution in Figure 3d, an average p-type doping of $0.45 \times 10^{13}\ cm^{-2}$ with a standard deviation of $0.11 \times 10^{13}\ cm^{-2}$ was evaluated for the CVD-grown 1L–MoS_2 on 4H–SiC.

MoS_2 doping can be due either to charge transfer phenomena with the substrate or overlayers or to the presence of native defects or impurities in the 2D crystal active as donor/acceptor levels. Typically, MoS_2 samples obtained by mechanical exfoliation or deposited by CVD on common insulating substrates (e.g., SiO_2, sapphire) exhibit n-type doping.[35–37] Although its origin is still matter of debate, this unintentional n-type doping has been associated by different authors to the large density of sulfur vacancies present in 2D MoS_2.[38–40] p-type behavior due to electron transfer to the substrate has been reported in the case of MoS_2 monolayers exfoliated on the surface of gold films.[29,41] On the other hand, substitutional p-type doping of MoS_2 has been obtained by introducing cation species (such as Nb,[42] Zn,[43] and Ta[44]) during growth. Alternatively, the incorporation of MoO_3 in the MoS_2 lattice results in p-type behavior, ascribed to the high work function of MoO_3 which causes a Fermi-level shift toward the valence band. This has been achieved by oxygen plasma post-treatments of exfoliated or CVD-grown MoS_2,[45,46] associated with unintentionally incorporated oxygen during MoS_2 deposition[47] or the presence of MoO_3 residuals in MoS_2 layers produced by sulfurization of predeposited MoO_x films.[18,25,48] In particular, we recently demonstrated the formation of a highly p-type-doped 1L MoS_2 on 4H–SiC by the sulfurization approach, in the presence of MoO_3 detected by XPS analyses[18]

Interestingly, no MoO_3 contributions were detected by XPS analyses on the CVD-grown MoS_2 sample. Hence, we expect that the p-type doping of MoS_2 on 4H–SiC deduced by Raman measurements can be related to charge transfer phenomena at the interface between these materials. To get a deeper understanding of the interface structure and electronic properties of the MoS_2/4H–SiC heterojunction, ab initio DFT calculations have been carried out considering different configurations of the system, starting from an ideal 1L–MoS_2/4H–SiC(0001) interface and subsequently considering the more realistic case of the SiC(0001) surface passivation by oxygen atoms.

Ideal or reconstructed SiC(0001) surfaces are usually characterized by the presence of Si dangling bonds, which tend to introduce electronic states within the 4H–SiC bandgap.[49–51] In this respect, **Figure 4**a shows the structural and electronic properties of the ideal, nonreconstructed 4H–SiC(0001) surface. The projected density of states calculated for wavevectors sampled along the close Γ–M–K–Γ Brillouin zone path (Figure 4a, lower panel) shows a half-filled quasiflat band within the SiC band gap, originating from the electronic contributions of mainly 3p orbitals of unsaturated Si dangling bonds. This band defines the Fermi level of the system and gives rise to mild n-type doping, due to its proximity with the conduction band of SiC. The simplest model of a MoS_2/4H–SiC(0001) heterostructure can be constructed through the direct interaction of this ideal surface with a single-layer MoS_2 sheet, resulting in minimum energy arrangement where sulfur atoms of the MoS_2 layer relax on top of the Si surface atoms, in agreement with previous calculations.[20] Figure 4b shows the geometry of the relaxed interface, with a calculated Si—S interface bond distance of 2.24 Å and an interface binding energy of 0.73 eV $atom^{-1}$. Both characteristics indicate a strong (covalent) MoS_2–SiC interaction, which is not consistent with the experimental evidence of a vdW gap at the MoS_2/4H–SiC(0001) interface (see Figure 1c). Electronically, such covalent interaction between the surface atoms totally passivates the surface Si dangling bonds and removes the respective states from the bandgap region. Furthermore, the system is characterized by an extremely high level of n-type doping. DFT calculations performed on a

© 2023 The Authors. physica status solidi (RRL) Rapid Research Letters published by Wiley-VCH GmbH
18626270, 2023, 10, Downloaded from https://onlinelibrary.wiley.com/doi/10.1002/pssr.202300218 by CochraneItalia, Wiley Online Library on [01/11/2023]. See the Terms and Conditions (https://onlinelibrary.wiley.com/terms-and-conditions) on Wiley Online Library for rules of use; OA articles are governed by the applicable Creative Commons License

18626270, 2023, 10, Downloaded from https://onlinelibrary.wiley.com/doi/10.1002/pssr.202300218 by CochraneItalia, Wiley Online Library on [01/11/2023]. See the Terms and Conditions (https://onlinelibrary.wiley.com/terms-and-conditions) on Wiley Online Library for rules of use; OA articles are governed by the applicable Creative Commons License

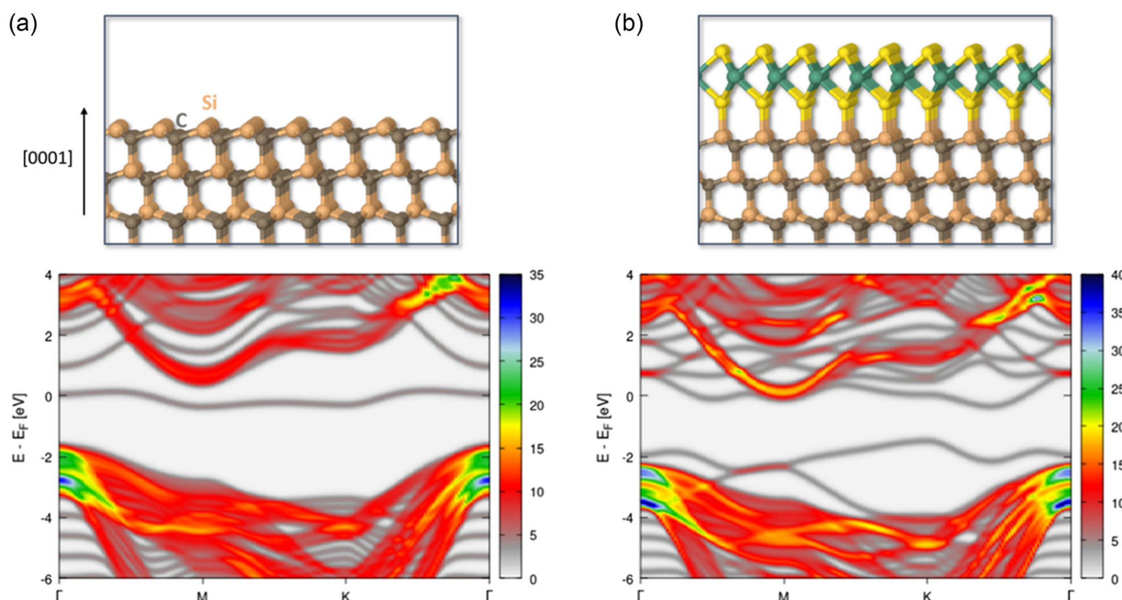

Figure 4. a) Atomic configuration of the ideal Si-terminated 4H–SiC(0001) surface (upper) and total wavevector-resolved projected density of states along the Γ–M–K–Γ Brillouin zone path (lower). b) Atomic configuration of the MoS_2/4H–SiC(0001) interface (upper) and total wavevector-resolved projected density of states along the Γ–M–K–Γ Brillouin zone path (lower). E_F refers to the calculated Fermi level of the systems.

free-standing monolayer MoS_2 (Figure S2, Supporting information) show that the latter should ideally be undoped. Hence, this n-type doping is a result of a strong hybridization between MoS_2 conduction band states with Si states originating from Si surface atoms, as illustrated in Figure S3, Supporting Information. This interaction shifts the Fermi level of the system to the (half-filled) conduction band of MoS_2. Overall, notwithstanding the covalent interface interaction, the MoS_2 bands are still clearly visible in the band structure of the system (Figure S3, Supporting Information), having though an indirect bandgap. We note here that this high level of n-type doping is independent of the number of MoS_2 layers that are present in the structure.

This ideal model of the MoS_2/4H–SiC(0001) system shows significant differences with respect to the experimental data, both regarding the type of interface bonding (covalent vs the experimentally deduced vdW interaction) and the doping of the MoS_2 layer (n-type vs the experimentally observed p-type doping). Such mismatch indicates that the structural/electronic characteristics of the MoS_2/4H–SiC(0001) heterojunction may require a level of modeling that takes into account an increased interface complexity or chemical variability.

In this respect, due to the presence of oxygen gas residues in the reactor chamber, a more realistic scenario can consider the occurrence of surface oxidation of the SiC substrate during the MoS_2 CVD growth process at 700 °C.[52] Starting from the previously discussed paradigm, one monolayer (1 ML) of oxygen can be directly introduced at the MoS_2/4H–SiC(0001) interface by inserting a single oxygen atom at the (1 × 1) interface model (resulting in a one-to-one ratio between O and Si surface atoms). This oxygen-passivated interface shows a totally different behavior with respect to the previously considered ideal case: 1) a van der Waals interface is now formed with a calculated minimum Si–S interface distance of 3.84 Å (see **Figure 5**a). Electronically, the system is now strongly p-doped (Figure 5b and S4, Supporting Information). The mechanism of p-type doping is explained by the presence of a high concentration of O atoms on the surface, which induces a rehybridization of C surface atoms below the Si-terminated surface from sp^3 to sp^2. This C rehybridization reduces the number of covalent bonds between surface Si and C atoms and, consequently, increases the number of available bonds that Si surface atoms can form with oxygen (Figure 5a). Structurally, O atoms acquire a "bridge" configuration between two surface Si atoms. The presence of sp^2-hybridized carbon at this interface has an important impact on the electronic properties of the system, as it introduces a half-filled C 2p band within the MoS_2 bandgap, which determines the Fermi level of the entire system (Figure 5c). It is important to note here that this doping mechanism is not directly related to the electronic contributions of the oxygen atoms at the 4H–SiC(0001)/MoS_2 interface, but to the structural modifications that these introduce on the 4H–SiC surface.

Besides the previously discussed models, where oxygen passivation of the 4H–SiC(0001) surface is either absent or present at a very high coverage, intermediate situations are likely to occur due to the noncontrollable nature of oxidation in 4H–SiC surfaces. In this respect, **Figure 6** shows the surface geometry and band structure of the 4H–SiC(0001)/MoS_2 heterostructure in the presence of ¼ ML and ½ ML of atomic oxygen coverage. We note that for these calculations, a 2 × 2 interface model has been considered. In both cases, the binding between the two parts of the heterostructure is weak, resulting in a van der Waals interaction. Contrary to the 1 ML coverage, the substrate maintains the sp^3 bond symmetry for all atoms and no C rehybridization phenomena are observed. In the ¼ ML case, the Fermi level stands in the middle of two intragap bands that originate from nonpassivated Si surface atoms with different structural arrangements due to the proximity of nearby oxygen. As these bands are closer to the conduction band of SiC, n-type

© 2023 The Authors. physica status solidi (RRL) Rapid Research Letters published by Wiley-VCH GmbH

18626270, 2023, 10, Downloaded from https://onlinelibrary.wiley.com/doi/10.1002/pssr.202300218 by CochraneItalia, Wiley Online Library on [01/11/2023]. See the Terms and Conditions (https://onlinelibrary.wiley.com/terms-and-conditions) on Wiley Online Library for rules of use; OA articles are governed by the applicable Creative Commons License

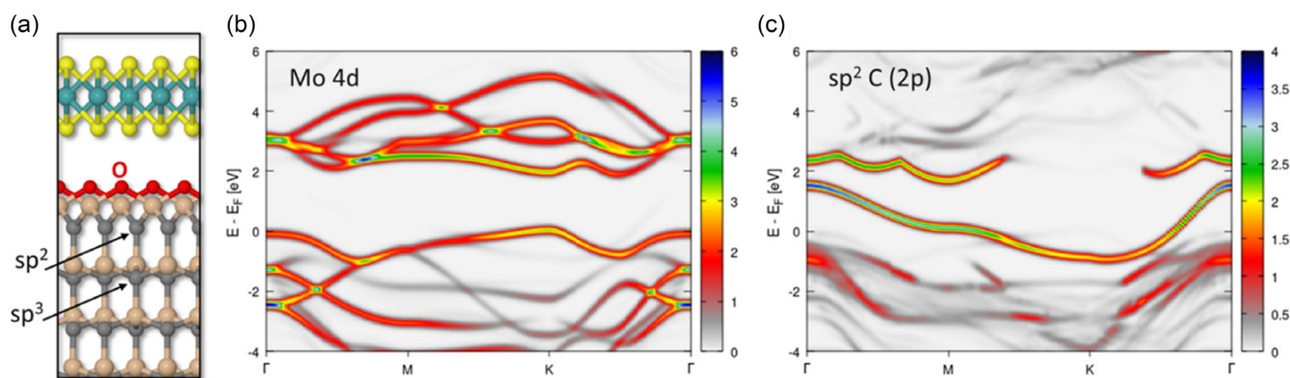

Figure 5. a) Atomic configuration of MoS_2 interface with the Si-terminated 4H–SiC surface fully passivated by oxygen atoms (1 ML surface coverage). b) Partial wavevector-resolved projected density of states along the Γ–M–K–Γ Brillouin zone path, showing the contributions of Mo 4*d* states. c) Partial wavevector-resolved projected density of states along the Γ–M–K–Γ Brillouin zone path, showing the contributions of C 2*p* states from sp^2-hybridized carbon atoms. E_F refers to the calculated Fermi level of the system.

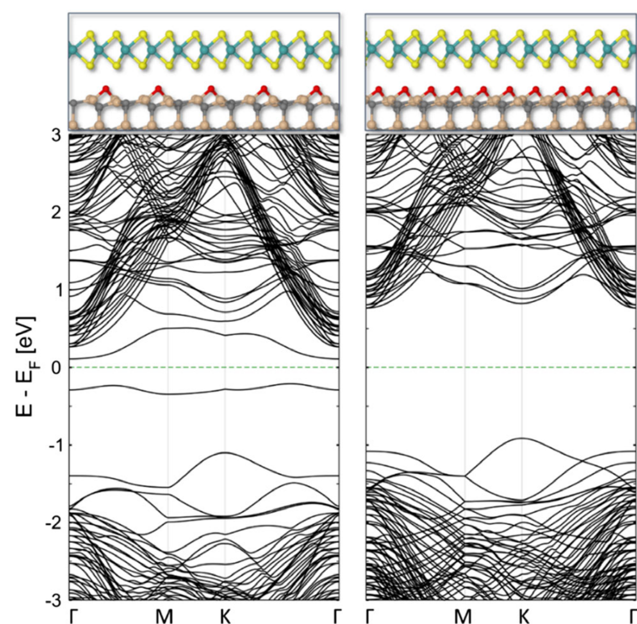

Figure 6. Band structure of the MoS_2/4H–SiC(0001) interface in the presence of a partially oxidized SiC surface: ¼ ML (left) and ½ ML (right). E_F refers to the calculated Fermi level of the two systems.

doping is expected. On the contrary, a ½ ML atomic oxygen coverage leads to a full passivation of surface Si dangling bonds, as O atoms form “bridge” configurations between two surface Si atoms. As a result, the interface does not control the Fermi level of the system. The latter may therefore be defined by other charge trapping or band shifting mechanisms, like the presence of defects (e.g., sulfur vacancies[53,54] or oxygen adatoms)[45] on the MoS_2 layer.

Finally, **Table 1** summarizes the results of the ab initio calculations for the ideal and oxidized 4H–SiC(0001)/MoS_2 heterostructure, depicting a rather complex scenario with respect to the doping of the MoS_2 sheet. Only in totally nonoxidized surface areas, a covalent interaction between the SiC substrate and MoS_2

Table 1. Binding energy per Si surface atom (in eV), minimum Si–S interface distance, and doping type for a 4H–SiC(0001)/MoS_2 interface with different oxygen coverages of the SiC surface.

Surf. O concentration	0 ML	¼ ML	½ ML	1 ML
Binding energy [eV]	−0.73	−0.16	−0.15	−0.16
Si–S int. distance [Å]	2.24	3.46	3.83	3.84
Doping type	n	n	–	p

is expected, whereas surface oxidation (even partial) should lead to van der Waals interfaces. The doping level should strongly depend on the oxygen surface coverage, ranging from highly n-doped for low coverages to highly p-doped for high oxygen surface coverages. This last aspect is important, as it implies that the p-type doping of the MoS_2 sheet, which is highly desirable for the realization of microelectronic devices, can be obtained not only by defect-creating processes like the plasma oxidation treatment of the MoS_2 layer,[45] but also through proper engineering of the supporting substrate.

3. Conclusion

In conclusion, we combined experimental characterizations and DFT calculations to describe 1L–MoS_2/4H–SiC heterostructures obtained by CVD. The triangular MoS_2 flakes exhibit rotational alignment with the (0001) basal plane and are subjected to a very small tensile strain (<0.1%), consistently with the very small lattice mismatch between the two crystals (<2.9%). Furthermore, p-type doping of $(0.45 \pm 0.11) \times 10^{13}\,\text{cm}^{-2}$ was deduced by Raman measurements. DFT calculations of equilibrium structure and electronic bands for the MoS_2/4H–SiC(0001) system were also performed, considering different levels of refinement of the model. A covalent bond, with a low-equilibrium Si–S distance $d_{Si-S} = 2.24$ Å between the two materials and n-type doping of the MoS_2 was predicted considering the simplest model without passivation of the 4H–SiC surface. In contrast, a more realistic description of the 2D/3D heterostructures was achieved

© 2023 The Authors. physica status solidi (RRL) Rapid Research Letters published by Wiley-VCH GmbH

considering passivation of the Si-terminated 4H–SiC surface by oxygen atoms. The presence of oxygen leads to vdW interaction between the MoS_2 and 4H–SiC (higher Si–S distance) and a tunable MoS_2 doping from n- to p-type moving from partial oxygen coverage (¼ ML and ½ ML) to full passivation (1 ML) of the SiC surface by oxygen atoms. The p-type doping of MoS_2 on the fully O-passivated surface was found to be caused by rehybridization of the C atoms below the Si surface from sp^3 to sp^2.

The results of these experimental and theoretical investigations provide a roadmap on the tunability of electronic properties in MoS_2/4H–SiC heterostructures by tailoring the interface structure.

4. Experimental Section

MoS_2 Growth and Characterizations: MoS_2 was grown by CVD in a two-heating zones furnace. The first zone held a crucible for the sulfur powder at 150 °C, while the second one held both a crucible for the molybdenum trioxide powder and for the 4H–SiC (0001) substrate at 700 °C. The process was carried out at base pressure for 1 h maintaining a continuous Ar gas flux of 100 sccm, to transport the evaporated sulfur from the first to the second zone.

Scanning electron microscopy images were acquired by ThermoFisher Scios 2 dual-beam microscope.

Furthermore, STEM analyses of the cross-sectioned MoS_2/SiC samples (lamella preparation with focused ion beam) were carried out with an aberration-corrected Thermofisher Themis 200 microscope.

Raman maps were carried out by a WiTec Alpha equipment, using a laser excitation at 532 nm, 1.5 mW power, and 100 × objective. Micro-Raman and micro-PL spectra were performed by a Horiba HR-Evolution micro-Raman system with a confocal microscope (100 × objective) and a laser excitation wavelength of 532 nm. Specifically, grating of 1800 lines mm^{-1} was used to acquire Raman spectra in a range from 150 to 650 cm^{-1}, while grating of 600 lines/mm was employed for the PL spectra. All the measurements were performed using a neutral density filter at 1% to avoid the MoS_2 degradation.

DFT Calculations: In order to study the structural and electronic properties of the 4H–SiC(0001)/MoS_2 interface in the presence of interfacial oxidation, we performed DFT calculations using the Quantum Espresso software suite.[52] In view of the experimental evidence of a van der Waals heterostructure for this system, we used the van der Waals exchange-correlation functional of Hamada,[55] which allowed for an accurate description of weakly chemisorbed bulk systems,[56] along with standard solid-state pseudopotentials[57,58] based on the Perdew–Burke–Ernzerhof functional[59] for the description of core electrons. The 4H–SiC substrate was modelled by a slab containing 16 bilayers of Si–C, whose bottom termination was passivated with hydrogen, whereas the top termination interacted with the MoS_2 layer. Considering the small mismatch between the lattice constants of MoS_2 and the surface lattice parameters of 4H–SiC(0001), a (1 × 1) model was constructed along the interface plane, consisting of a periodically replicated quasicommensurate interface between a SiC(0001) unit area (with surface lattice parameters $a = b = 3.116$ Å) and a slightly compressed MoS_2 unit cell (with a compressive strain of 1.6%). For partially oxidized interfaces instead, a (2 × 2) interface model was implemented, to account for the presence of different surface oxygen coverages. Convergence was achieved with a plane-wave cutoff kinetic energy of 50 Ry and an augmented charge density cutoff of 400 Ry, using (12 × 12 × 1) and (6 × 6 × 1) Monkhorst–Pack grids[60] for the sampling of the Brillouin zone in the case of the (1 × 1) and (2 × 2) models, respectively. A vacuum space of at least 20 Å perpendicular to the 4H–SiC(0001)/MoS_2 interface was inserted in the simulation cell to avoid spurious interactions between the periodic replicas of the system toward the [0001] direction. The binding energy of the MoS_2 sheet on various pure and oxidized substrates was calculated as $E_b = E_{tot} - (E_{SiC} + E_{MoS2})$, where E_{tot} was the ground state energy of the 4H–SiC(0001)/MoS_2 interface and E_{SiC}/E_{MoS2} the respective energies of the separated parts of the heterostructure.

Supporting Information

Supporting Information is available from the Wiley Online Library or from the author.

Acknowledgements

S. Di Franco (CNR-IMM) is acknowledged for his expert assistance with samples preparation. This work was supported, in part, by MUR in the framework of the FlagERA JTC 2019 project ETMOS. Funding for travels from CNR/HAS (2023-25) bilateral project GHOST-III is acknowledged. The authors from CNR and University of Palermo acknowledge funding by MUR within the project "Samothrace" (PNRR-M4C2, ECS_00000022).

Conflict of Interest

The authors declare no conflict of interest.

Data Availability Statement

The data that support the findings of this study are available from the corresponding author upon reasonable request.

Keywords

chemical vapor deposition, density functional theory, doping, MoS_2, Raman, SiC

Received: June 17, 2023
Revised: July 19, 2023
Published online: August 1, 2023

[1] Q. H. Wang, K. Kalantar-Zadeh, A. Kis, J. N. Coleman, M. S. Strano, *Nat. Nanotechnol.* **2012**, *7*, 699.
[2] K. F. Mak, C. Lee, J. Hone, J. Shan, T. F. Heinz, *Phys. Rev. Lett.* **2010**, *105*, 136805.
[3] A. Splendiani, L. Sun, Y. Zhang, T. Li, J. Kim, C. Y. Chim, G. Galli, F. Wang, *Nano Lett.* **2010**, *10*, 1271.
[4] O. Lopez-Sanchez, D. Lembke, M. Kayci, A. Radenovic, A. Kis, *Nat. Nanotechnol.* **2013**, *8*, 497.
[5] B. Radisavljevic, M. B. Whitwick, A. Kis, *ACS Nano* **2011**, *5*, 9934.
[6] J. Hu, L. Yu, J. Deng, Y. Wang, K. Cheng, C. Ma, Q. Zhang, W. Wen, S. Yu, Y. Pan, J. Yang, H. Ma, F. Qi, Y. Wang, Y. Zheng, M. Chen, R. Huang, S. Zhang, Z. Zhao, J. Mao, X. Meng, Q. Ji, G. Hou, X. Han, X. Bao, Y. Wang, D. Deng, *Nat. Catal.* **2021**, *4*, 242.
[7] H. Li, Z. Yin, Q. He, H. Li, X. Huang, G. Lu, D. W. H. Fam, A. L. Y. Tok, Q. Zhang, H. Zhang, *Small* **2012**, *8*, 63.
[8] D. Jariwala, T. J. Marks, M. C. Hersam, *Nat. Mater.* **2017**, *16*, 170.
[9] Y. Liu, N. O. Weiss, X. Duan, H. C. Cheng, Y. Huang, X. Duan, *Nat. Rev. Mater.* **2016**, *1*, 16042.
[10] C.-Y. Huang, C. Chang, G.-Z. Lu, W.-C. Huang, C.-S. Huang, M.-L. Chen, T.-N. Lin, J. L. Shen, T.-Y. Lin, *Appl. Phys. Lett.* **2018**, *112*, 233106.
[11] Y. Wu, Z. Li, K.-W. Ang, Y. Jia, Z. Shi, Z. Huang, W. Yu, X. Sun, X. Liu, D. Li, *Photonics Res.* **2019**, *7*, 1127.

© 2023 The Authors. physica status solidi (RRL) Rapid Research Letters published by Wiley-VCH GmbH

18626270, 2023, 10, Downloaded from https://onlinelibrary.wiley.com/doi/10.1002/pssr.202300218 by Cochraneltalia, Wiley Online Library on [01/11/2023]. See the Terms and Conditions (https://onlinelibrary.wiley.com/terms-and-conditions) on Wiley Online Library for rules of use; OA articles are governed by the applicable Creative Commons License

[12] Y. Xiao, L. Min, X. Liu, W. Liu, U. Younis, T. Peng, X. Kang, X. Wu, S. Ding, D. W. Zhang, *Nanophotonics* **2020**, *9*, 3035.
[13] K. Zhang, M. Peng, A. Yu, Y. Fan, J. Zhai, Z. L. Wang, *Mater. Horiz.* **2019**, *6*, 826.
[14] S. Krishnamoorthy, E. W. Lee, C. H. Lee, Y. W. Zhang, W. D. McCulloch, J. M. Johnson, J. Hwang, Y. Y. Wu, S. Rajan, *Appl. Phys. Lett.* **2016**, *109*, 183505.
[15] D. Ruzmetov, K. Zhang, G. Stan, B. Kalanyan, G. R. Bhimanapati, S. M. Eichfeld, R. A. Burke, P. B. Shah, T. P. O'Regan, F. J. Crowne, A. G. Birdwell, J. A. Robinson, A. V. Davydov, T. G. Ivanov, *ACS Nano* **2016**, *10*, 3580.
[16] E. W. Lee II, L. Ma, D. N. Nath, C. H. Lee, A. Arehart, Y. Wu, S. Rajan, *Appl. Phys. Lett.* **2014**, *105*, 203504.
[17] F. Giannazzo, S. E. Panasci, E. Schilirò, P. Fiorenza, G. Greco, F. Roccaforte, M. Cannas, S. Agnello, A. Koos, B. Pécz, M. Španková, Š. Chromik, *Adv. Mater. Interfaces* **2023**, *10*, 2201502.
[18] F. Giannazzo, S. E. Panasci, E. Schilirò, F. Roccaforte, A. Koos, M. Nemeth, B. Pécz, *Adv. Mater. Interfaces* **2022**, *9*, 2200915.
[19] J. Bradford, A. Zaganelli, D. Qi, N. Zebardastan, M. Shafiei, J. MacLeod, N. Motta, *Appl. Surf. Sci.* **2021**, *552*, 149303.
[20] B. Mao, X. Lv, G. Zhao, S. Xing, J. Tang, H. Huang, G. Liu, Y. Gao, *Appl. Phys. Lett.* **2022**, *121*, 051601.
[21] D. Dumcenco, D. Ovchinnikov, K. Marinov, P. Lazic, M. Gibertini, N. Marzari, O. L. Sanchez, Y. C. Kung, D. Krasnozhon, M. W. Chen, S. Bertolazzi, P. Gillet, A. F. i Morrali, A. Radenovic, A. Kis, *ACS Nano* **2015**, *9*, 4611.
[22] H. Yu, M. Liao, W. Zhao, G. Liu, X. J. Zhou, Z. Wei, X. Xu, K. Liu, Z. Hu, K. Deng, S. Zhou, J. A. Shi, L. Gu, C. Shen, T. Zhang, L. Du, L. Xie, J. Zhu, W. Chen, R. Yang, D. Shi, G. Zhang, *ACS Nano* **2017**, *11*, 12001.
[23] S. E. Panasci, E. Schilirò, F. Migliore, M. Cannas, F. M. Gelardi, F. Roccaforte, F. Giannazzo, S. Agnello, *Appl. Phys. Lett.* **2021**, *119*, 093103.
[24] J. Y. Lee, J. H. Kim, Y. Jung, J. C. Shin, Y. Lee, K. Kim, N. Kim, A. M. van der Zende, J. Son, G. H. Lee, *Commun. Mater.* **2021**, *2*, 80.
[25] S. E. Panasci, A. Koos, E. Schilirò, S. Di Franco, G. Greco, P. Fiorenza, F. Roccaforte, S. Agnello, M. Cannas, F. M. Gelardi, A. Sulyok, M. Nemeth, B. Pécz, F. Giannazzo, *Nanomaterials* **2022**, *12*, 182.
[26] S. Mignuzzi, A. J. Pollard, N. Bonini, B. Brennan, I. S. Gilmore, M. A. Pimenta, D. Richards, D. Roy, *Phys. Rev. B.* **2015**, *91*, 195411.
[27] C. Lee, H. Yan, L. E. Brus, T. F. Heinz, J. Hone, S. Ryu, *ACS Nano* **2010**, *4*, 2695.
[28] A. Michail, N. Delikoukos, J. Parthenios, C. Galiotis, K. Papagelis, *Appl. Phys. Lett.* **2016**, *108*, 173102.
[29] S. E. Panasci, E. Schilirò, G. Greco, M. Cannas, F. M. Gelardi, S. Agnello, F. Roccaforte, F. Giannazzo, *ACS Appl. Mater. Interfaces* **2021**, *13*, 31248.
[30] W. H. Chae, J. D. Cain, E. D. Hanson, A. A. Murthy, V. P. Dravid, *Appl. Phys. Lett.* **2017**, *111*, 143106.
[31] R. J. Angel, M. Murri, B. Mihailova, M. Alvaro, *Z. Kristallogr. - Cryst. Mater.* **2019**, *234*, 129.
[32] N. Ferralis, *J. Mater. Sci.* **2010**, *45*, 5135.
[33] B. Chakraborty, A. Bera, D. V. S. Muthu, S. Bhowmick, U. V. Waghmare, A. K. Sood, *Phys. Rev. B* **2012**, *85*, 161403.
[34] D. Lloyd, X. Liu, J. W. Christopher, L. Cantley, A. Wadehra, B. L. Kim, J. S. Bunch, *Nano Lett.* **2016**, *16*, 5836.
[35] B. Radisavljevic, A. Radenovic, J. Brivio, V. Giacometti, A. Kis, *Nat. Nanotechnol.* **2011**, *6*, 147.
[36] W. Zhang, J. K. Huang, C. H. Chen, Y. H. Chang, Y. J. Cheng, L. J. Li, *Adv. Mater.* **2013**, *25*, 3456.
[37] G. Plechinger, J. Mann, E. Preciado, D. Barroso, A. Nguyen, J. Eroms, C. Shüller, L. Bartels, T. Korn, *Semicond. Sci. Technol.* **2014**, *29*, 064008.
[38] J. Yang, H. Kawai, C. P. Y. Wong, K. E. J. Goh, *J. Phys. Chem. C* **2019**, *123*, 2933.
[39] A. Singh, A. K. Singh, *Phys. Rev. B* **2019**, *99*, 121201.
[40] H. Lu, A. Kummel, J. Robertson, *APL Mater.* **2018**, *6*, 066104.
[41] E. Schilirò, S. E. Panasci, A. M. Mio, G. Nicotra, S. Agnello, B. Pecz, G. Z. Radnoczi, I. Deretzis, A. La Magna, F. Roccaforte, R. Lo Nigro, F. Giannazzo, *Appl. Surf. Sci.* **2023**, *630*, 157476.
[42] J. Suh, T. E. Park, D. Y. Lin, D. Fu, J. Park, H. J. Jung, Y. Chen, C. Ko, C. Jang, Y. Sun, R. Sinclair, J. Chang, S. Tongay, J. Wu, *Nano Lett.* **2014**, *14*, 6976.
[43] E. Z. Xu, H. M. Liu, K. Park, Z. Li, Y. Losovyj, M. Starr, M. Werbianskyj, H. A. Fertig, S. X. Zhang, *Nanoscale* **2017**, *9*, 3576.
[44] M. Li, X. Wu, W. Guo, Y. Liu, C. Xiao, T. Ou, Y. Zheng, Y. Wang, *J. Mater. Chem. C* **2022**, *10*, 7662.
[45] F. Giannazzo, G. Fisichella, G. Greco, S. Di Franco, I. Deretzis, A. La Magna, C. Bongiorno, G. Nicotra, C. Spinella, M. Scopelliti, B. Pignataro, S. Agnello, F. Roccaforte, *ACS Appl. Mater. Interfaces* **2017**, *9*, 23164.
[46] S. Wu, Y. Zeng, X. Zeng, S. Wang, Y. Hu, W. Wang, S. Yin, G. Zhou, W. Jin, T. Ren, Z. Guo, J. Lu, *2D Mater.* **2019**, *6*, 025007.
[47] A. T. Neal, R. Pachter, S. Mou, *Appl. Phys. Lett.* **2017**, *110*, 193103.
[48] F. Giannazzo, S. E. Panasci, E. Schilirò, G. Greco, F. Roccaforte, G. Sfuncia, G. Nicotra, M. Cannas, S. Agnello, E. Frayssinet, Y. Cordier, A. Michon, A. Koos, B. Pécz, *Appl. Surf. Sci.* **2023**, *631*, 157513.
[49] U. Starke, J. Bernhardt, J. Schardt, K. Heinz, *Surf. Rev. Lett.* **1999**, *6*, 1129.
[50] J. Pollmann, P. Krüger, *J. Phys.: Condens. Matter* **2004**, *16*, S1659.
[51] I. Deretzis, A. La Magna, *Phys. Rev. B* **2011**, *84*, 235426.
[52] P. Giannozzi, S. Baroni, N. Bonini, M. Calandra, R. Car, C. Cavazzoni, D. Ceresoli, L. C. Guido, M. Cococcioni, I. Dabo, A. D. Corso, S. de Gironcoli, S. Fabris, G. Fratesi, R. Gebauer, U. Gerstmann, C. Gougoussis, A. Kokalj, M. Lazzeri, L. Martin-Samos, N. Marzari, F. Mauri, R. Mazzarello, S. Paolini, A. Pasquarello, L. Paulatto, C. Sbraccia, S. Scandolo, G. Sclauzero, A. P. Seitsonen, et al., *J. Phys. Condens. Matt.* **2009**, *21*, 395502.
[53] J. Y. Noh, H. Kim, Y. S. Kim, *Phys. Rev. B* **2014**, *89*, 205417.
[54] H. P. Komsa, A. V. Krasheninnikov, *Phys. Rev. B* **2015**, *91*, 125304.
[55] I. Hamada, *Phys. Rev. B* **2014**, *89*, 121103.
[56] K. Berland, V. R. Cooper, K. Lee, E. Schröder, T. Thonhauser, P. Hyldgaard, B. I. Lundqvist, *Rep. Prog. Phys.* **2015**, *78*, 066501.
[57] G. Prandini, A. Marrazzo, I. E. Castelli, N. Mounet, N. Marzari, *npj Comput. Mater.* **2018**, *4*, 72.
[58] K. Lejaeghere, et al., *Science* **2016**, *351*, aad3000.
[59] J. P. Perdew, K. Burke, M. Ernzerhof, *Phys. Rev. Lett.* **1996**, *77*, 3865.
[60] H. J. Monkhorst, J. D. Pack, *Phys. Rev. B* **1976**, *13*, 5188.

© 2023 The Authors. physica status solidi (RRL) Rapid Research Letters published by Wiley-VCH GmbH

18626270, 2023, 10, Downloaded from https://onlinelibrary.wiley.com/doi/10.1002/pssr.202300218 by CochraneItalia, Wiley Online Library on [01/11/2023]. See the Terms and Conditions (https://onlinelibrary.wiley.com/terms-and-conditions) on Wiley Online Library for rules of use; OA articles are governed by the applicable Creative Commons License